ORIGINAL ARTICLE

Numerical predictions of orthogonal cutting–induced residual stress of super alloy Inconel 718 considering dynamic recrystallization

Emadedin Soufian[1] · Roya Darabi[2,3] · Mustapha Abouridouane[1] · Ana Reis[2,3] · Thomas Bergs[1]

Abstract

Manufacturing processes, such as machining, can produce residual stresses in products. Residual stress and its distribution can be the main factor influencing the fatigue life of machined components and has already been the subject of many experimental and numerical studies. The high-temperature condition, as a result of machining, makes a change in the microstructural properties of the material and consequently affect the mechanical properties of the workpiece. A major metal component of aircraft structure and engine components is nickel-based alloys due to their resistance to heat, corrosion, thermal fatigue, thermal shock, creep, and erosion. When these critical structural components in the aerospace industry are manufactured with the objective to reach high-reliability levels, surface integrity is one of the most relevant parameters used for evaluating the quality of finish-machined surfaces. The residual stresses and surface alterations including white layer, depth of work hardening, micro-cracks, and oxidation induced by machining of nickel-based alloys are extremely critical due to safety and sustainability concerns. Integrated Computational Materials Engineering (ICME) links physics-based models to predict the performance of materials based on their processing history. The Johnson–Mehl–Avrami-Kolmogrov (JMAK) model is used to develop a microstructure-based modeling approach that takes into account dynamic recrystallization (DRX) that causes grain size changes. Allied with that, a grain size parameter on the flow stress behavior of the material is considered by adding a grain size-dependent term to the traditional Johnson–Cook (JC) model as a novel framework. The impact of the simulation of the orthogonal cutting process is implemented in a finite element method (FEM) model–based commercial software, ABAQUS-explicit, with a coupled Euler-Lagrangian (CEL) approach. By relying on the VUHARD user subroutine capabilities with Fortran language, ABAQUS-explicit can be steered to model the material behavior considering the term of DRX. The forecast capability of the developed model is assessed by comparison of the results by changing the depth of cut and cutting edge radius effect on the residual stress. Then, the correlation between the grain size evolution and temperature distribution by changing the cutting velocity is investigated.

Keywords Residual stress · Dynamic recrystallization · Finite element method · Coupled Euler-Lagrangian · Inconel 718

Abbreviations

ICME	Integrated Computational Materials Engineering
JMAK	Johnson-Mehl-Avrami-Kolmogrov
JC	Johnson-Cook
FEM	Finite element method
FE	Finite element
CEL	Coupled Euler-Lagrangian
DRX	Dynamic recrystallization

✉ Emadedin Soufian
emadedin.soufian@rwth-aachen.de

1 Laboratory for Machine Tools and Production Engineering (WZL), RWTH Aachen University, Aachen, Germany

2 Institute of Science and Innovation in Mechanical and Industrial Engineering (INEGI), FEUP Campus, Rua Dr. Roberto Frias, 400, 4200-465 Porto, Portugal

3 Faculty of Engineering of University of Porto (FEUP), Rua Dr. Roberto Frias, 4200-465 Porto, Portugal

1 Introduction

Over the last few decades, a wide range of nickel alloys has been used in high-temperature industrial sectors to satisfy specific material performance goals for a few structurally and ecologically demanding applications [1]. Its corrosion-resistant capabilities make nickel alloys a welcome choice in high-endurance applications [2]. Corrosion resistance makes nickel-based alloys ideal for nuclear, marine, petrochemical, and other such industrial applications [3]. The heat resistance capabilities of

nickel-based alloys also make them useful for other industrial purposes [4]. According to the aforementioned points, a hard turning can be considered as a practical machining process and offers many advantages, including direct machining of the workpiece in the hardened state, greater flexibility and cutting performance, and the elimination of the grinding process [5]. The existing residual stress state of the component may be changed due to mechanical, thermal, or chemical factors [6]. The mechanical factor is the material removal process, the thermal factor is the work done by friction, and the chemical factor is the possible reactions caused by cutting fluids [7]. Mechanical effects and plastic deformations of the machining processes change the surface finish and microstructure [8]. Thermal effects are created by the process, causing a change in the dislocation density and distribution and surface integrity [9]. Besides, pressure and the cooling temperature are essential effects that contribute to the formation of residual stresses [10]. The combination of these effects and other parameters of the machining like phase changing may form cracks on the surface of the component [11]. The cracks are the consequence of residual stresses, which are created because of plastic deformation and phase changes [12]. Phase changes are caused by local heating phenomena. Local heat increases due to friction and other abrasive effects of the machining. Tensile residual stresses are formed partially because of local heating [13]. Machining residual stress origins from thermal and mechanical factors affect the reliability and lifetime of the component [14, 15]. It has been well documented that the changes in cutting speed would change the residual stress depth profiles [16]. M´Saoubi et al. illustrated that the lowest cutting speed leads to the lowest residual stress, while the highest cutting speed can cause a great temperature gradient in the tool and workpiece that produces the highest residual stress on the workpiece [17]. Elsheikh et al. studied the induced residual stress imperfection during the machining operations and its consequence that can lead to lower fatigue life; hence, these phenomena should be analyzed and controlled. The affected layer is generated within the machined surface layer through the cutting process [14]. Hua and Liu illustrated that the cutting conditions such as the cutting edge radius, feed rate, and shape of cutting edge at the finishing operation affect residual stress, surface hardness, and surface roughness [18]. A previous research by Sasahara focused on the interaction of the cutting conditions with the machined surface property to some extent. Besides, the machining conditions' effect on fatigue life is investigated through several fatigue tests using the specimen finished under various cutting conditions. It is shown that it is possible to get a longer fatigue life for machined parts than the virgin material or the carefully finished material without the affected layer, only by setting the proper cutting conditions. Such a situation was realized when the generated residual stress was small, and the induced surface hardness was high. A longer fatigue life for the machined components can be obtained by applying such cutting conditions as a low feed rate, a small corner radius, and

a chamfered innovative tool [19]. Schijve studied the various sources of residual stress present as (i) inhomogeneous plastic deformation, in many cases at notches, (ii) production processes especially cutting process, and (iii) heat treatment [20].

In this research, according to ICME (Integrated Computational Materials Engineering), the development and supply of an innovative microstructure-based modeling approach are studied to predict the residual stresses induced in the machined surface during orthogonal cutting Inconel 718 with a geometrically determined cutting edge. Besides, grain size evolution is investigated by tracking temperature in the process taking advantage of the Johnson–Mehl–Avrami-Kolmogrov (JMAK) model relying on the capabilities of FORTRAN language in developing the user subroutine of VUHARD in the ABAQUS-explicit framework. The paper is organized as follows: Sect. 2 contains the aim and objective of the study. Section 3 includes the numerical approach, consisting of governing equations of the dynamic recrystallization (DRX) concept in material modeling. Section 4 focuses on the finite element (FE) modeling of the orthogonal cutting process using ABAQUS-explicit, which entails the implementation of formulation in the VUHARD user interface subroutine and utilized algorithm. Subsequently, in Sect. 5 the results from the proposed numerical method are presented and the effective input parameters vary to assess the efficiency of the model. In Sect. 6, conclusions are drawn and summarized.

2 Challenge and opportunities

The overall objective of the paper is the development of an innovative microstructure-based modeling approach to predict the residual stresses induced in the machined surface during orthogonal cutting Inconel 718 with a geometrically determined cutting edge. Another target of the current study is to forecast the grain size evolution based on dynamic recrystallization. At present, there is no ready constitutive material model in ABAQUS to explain the effect of DRX and grain size on the residual stress completely and track these features in an in situ process. The nuclear focus of this paper is to develop the constitutive material model that can truly explain the relation of the input variables, such as cutting velocity and depth of cut, to the output parameters such as residual stress, temperature distribution, and grains size evolution. Then the link between the fatigue life of the machined component with the residual stress induced by the cutting process is investigated by keeping track of heat flux and temperature. In line with monitoring, dynamic temperature-displacement analysis is selected to survey the temporal progression in parallel to other parameters related to the displacement, such as various kinds of stress and strain.

Table 1 Modified JC model parameters for Inconel 718 [23]

A_{hp}	$K_{hp}(MPa/\sqrt{\mu m})$	B	C	m	n	$T_m(C^\circ)$	ε_0
378	298.4	1370	0.02	1.03	1.64	1300	1

3 Mathematical material modeling considering DRX

To define a suitable material model for Inconel 718, the grain size effect on the material flow stress behavior is included by adding grain size–dependent terms into the traditional JC model [21, 22]. The JMAK model calculates the recrystallized volume fraction and grain size as a function of strain, strain rate, and time. The average grain size is calculated with a rule of the mixture by volume. It is well documented that the traditional model assumes all JC parameters to be constants, which does not consider the recrystallization effect. However, at a higher temperature, the augmented grain size will reduce the flow stress. The Hall–Petch equation describes the relationship between A_{hp}, K_{hp}, and d in Eq. (1).

$$A = A_{hp} + K_{hp}d^{-0.5} \tag{1}$$

where d is the average grain size and A_{hp} and K_{hp} are material constants. Then the modified JC flow stress model can be presented as shown in Eq. (2).

$$\sigma = \left(A_{hp} + K_{hp}d^{-0.5} + B\dot{\varepsilon}^n\right)\left(1 + C\ln\frac{\dot{\varepsilon}}{\dot{\varepsilon}_0}\right)\left\{1 - (\frac{T - T_0}{T_m - T_0})^m\right\} \tag{2}$$

where B, C, m, and n are material constants; ε is the plastic strain; $\dot{\varepsilon}$ is the plastic strain rate; ε_0 is the reference strain rate, selected to be $1(s^{-1})$; T_m is the melting temperature of Inconel 718; T_0 is the environment temperature; and T is the temperature of the chip or shear plane. Table 1 represents the parameters for modified JC model parameters for Inconel 718 [23].

As reported by Johansson et al. [24], the machining process could significantly change the workpiece material microstructure. The initial workpiece material consists of equiaxed γ grains with an average grain size of 5.9μm [25]. The temperature and large strain effect dominate the grain growth in the machining of Inconel 718. To decide on the grain size, the JMAK model [26] is used to describe the DRX process of crystalline material. Based on the assumption that nucleation and grain growth are randomly distributed, the average grain size d could then be expressed as Eq. (3).

$$d = d_{drex}X_{drex} + d_0(1 - X_{drex}) \tag{3}$$

where d_0 is the initial average grain size, d_{drex} is the dynamically recrystallized average grain size, and X_{drex} is the recrystallized volume fraction. When ε is larger than a threshold value $a_2\varepsilon_p$, the DRX will occur. ε_p is the peak strain as Eq. (4).

$$\varepsilon_p = a_1 d_0^{h_1}\dot{\varepsilon}_0^{m_1}\exp\left(\frac{Q_{act}m_1}{RT}\right) + c_1 \tag{4}$$

where R is the gas constant, Q_{act} is the activation energy, and a_1, h_1, m_1, and c_1 are material constants. The peak strain parameter for JMAK model is shown in Table 2.

The recrystallized volume fraction is defined with the Avrami equation as Eq. (5).

$$X_{drex} = 1 - \exp\left[-\beta_d\left(\frac{\dot{\varepsilon} - a_{10}\varepsilon_p}{\varepsilon_{0.5}}\right)^{k_d}\right] \tag{5}$$

where β_d, a_{10}, and k_d are material constants (Table 3) and $\varepsilon_{0.5}$ is the strain that gives $X_{drex} = 0.5$, which is calculated as Eq. (6).

$$\varepsilon_{0.5} = a_5 d_0^{h_5}\varepsilon^{n_5}\dot{\varepsilon}^{m_5}\exp\left[\frac{Q_{act}m_5}{RT}\right] + c_5 \tag{6}$$

where a_5, h_5, n_5, m_5, and c_5 are material constants in Table 4. The dynamically recrystallized average grain size d_{drex} is given by Eq. (7).

$$d_{drex} = a_8 d_0^{h_8}\varepsilon^{n_8}\dot{\varepsilon}^{m_8}\exp\left[\frac{Q_{act}m_8}{RT}\right] + c_8 \tag{7}$$

where a_8, h_8, n_8, m_8, and c_8 are material constants in Table 5; the results from X_{drex} and d_{drex} provide the average grain size in d. Then the modified JC flow stress model in σ is computable. The modified JC flow stress model parameters are obtained from Jafarian et al. [27]. The JMAK model parameters are obtained from Huang et al. [23], Reyes et al. [28], and Loyda [29], as listed in the following tables. The initial grain size d_0 is assumed to be 5.9 μm from microscopic observation.

Table 2 Peak strain parameter for JMAK model for Inconel 718 [23]

Peak strain parameters	$a_1 d_0^{h_1}$	m_1	$Q_{act}m_1$	c_1
Value	$0.4659e-2$	0.1238	$49520(Jmol^{-1})$	0

Table 3 DRX kinematics parameters of JAMK model for Inconel718 [23]

Kinematics parameters	β_d	k_d	a_{10}	a_2
Value	0.693	2	0.8	0.8

Table 4 Required strain parameters of JAMK model for Inconel 718 [23]

Strain parameters	a_5	h_5	n_5	m_5	$Q_{act}m_5$	c_5
Value	$5.43e-9$	0	-1.42	-0.408	$196,000(Jmol^{-1})$	0

Table 5 DRX grain size parameters of JMAK model for Inconel 718 [23]

Grain size parameters	a_8	h_8	n_8	m_8	$Q_{act}m_8$	c_8
Value	$4.85e10$	0	-0.4	-0.028	$-240,000(Jmol^{-1})$	0

4 Numerical approach

4.1 Orthogonal cutting FE modeling

Hard machining is a complicated process to model due to the elevated temperatures, strain rates, and extensive plastic deformations. The main problem hereby is the distorted elements during chip formation. There are several techniques to handle this problem in FE simulations, like (i) element deletion (explicit), (ii) CEL method (explicit), and (iii) re-meshing with the updated Lagrangian (UL) method (implicit). Due to the lack of possibility in heat transient from the rim zone to the underlayers in the element deletion approach, this model is not suitable for the DRX concept. Regarding the study by Tekkaya et al. [30], the implemented re-meshing algorithm in ABAQUS is not good enough to model the machining process.

In this study, CEL is assessed because of the continuous contact between the elements themselves and the cutting

Fig. 1 Schematic orthogonal cutting model with the CEL method in ABAQUS-explicit. **a** Initial and boundary conditions of an orthogonal cutting. **b** Modeling by FEM
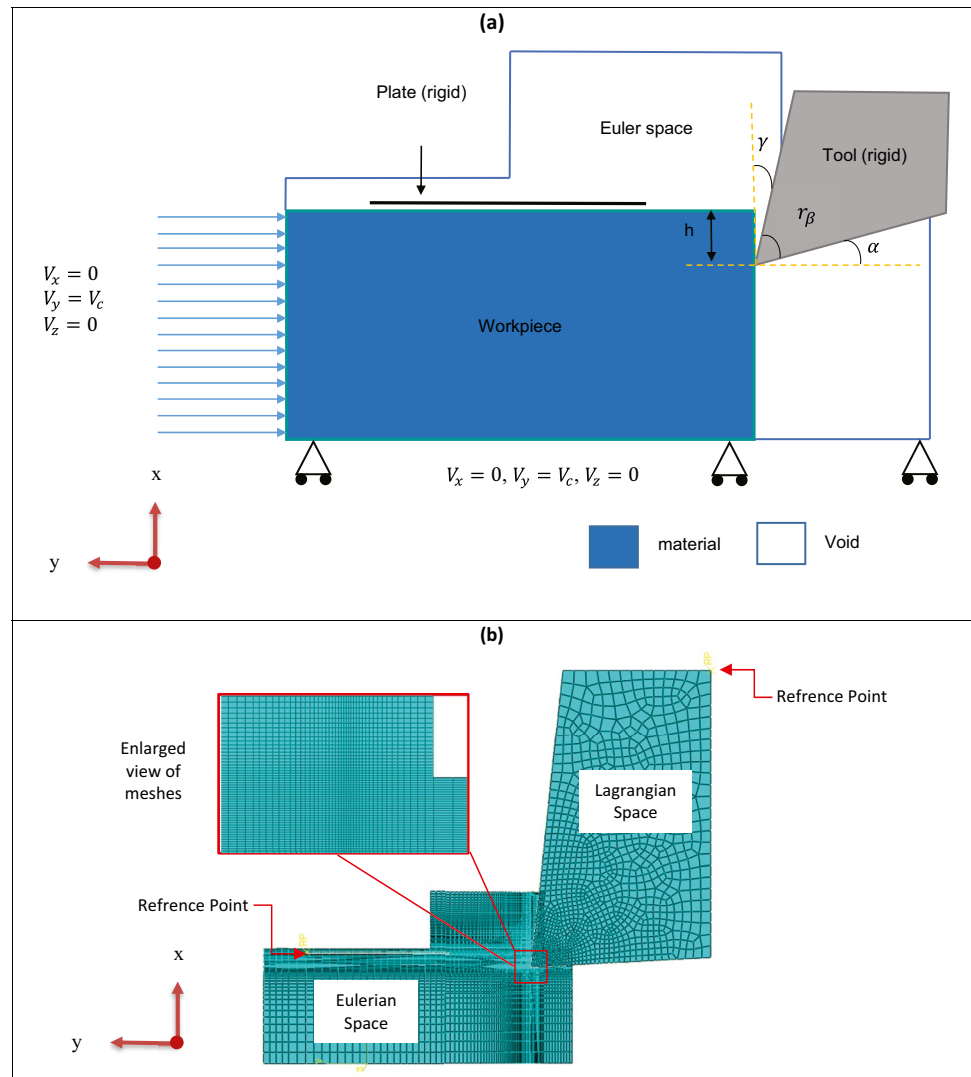
Table 6 Tool geometry and cutting parameters

Property	Notation	Value	Unit
Clearance/flank angle	α	3	°
Rake angle	γ	6	°
Cutting edge radius	r_β	1, 70	µm
Cutting speed	V_c	50, 100, 150	$^m/_{min}$
Depth of cut	h	0.06, 0.12, 0.2	mm

Table 7 Material specification of the cutting tool (carbide) and In718

Materials	Density (g/cm³)	Young module E(N/mm²)	ϑ
tool (carbide)	15.6	$6.0 * 10^6$	0.22
	Density (g/cm³)	Inelastic heat fraction	
In718	8.19	0.9	

Table 8 Thermo-physical properties of cutting tool (carbide)

Temp.(K)	Conductivity (W/m.K)	Specific heat (N.mm/g.K)
293.15	100	213, 000
773.15	68.9	250, 000
873.15	66.7	276, 000
1773.15	64.8	285, 000

tool, which makes it suitable for the calculation of dynamically recrystallized grain size on the workpiece surface in contact with the tool. To deal with the mesh problems, the Eulerian meshing approach is used for the workpiece to cover the excessive element distortion phenomena in cutting while the Lagrangian mesh type is dedicated to the cutting tool. The Eulerian mesh is fixed in space and the material moves through it, while the nodes of an element in the Lagrangian mesh move with the material and a mesh deformation takes place. Figure 1a and b show the schematic orthogonal-cutting model with the CEL method in ABAQUS-explicit.

The element type EC3D8RT, which stands for thermally connected linear brick elements with eight nodes and one Gaussian point, is used to mesh the workpiece. The tool and plate were meshed by utilizing the element type C3D8T, which describes an eight-node trilinear displacement and temperature element with eight Gaussian points. Tool geometry and cutting parameters used in the simulations and experiments are listed in Table 6. It is worth to be noted that the model is 3D with a thickness of one element, 2µm, in width (z-direction).

To represent the DRX on the surface layer and the resulting chip geometry in Euler space successfully, the mesh size must be fine enough. For this reason, the mesh size of the work piece in this model was set to 50µm, while the mesh size on the cutting edge was 9µm and for some run fine to 4µm. Three steps are considered for the process: the first one is dynamic temperature-displacement-explicit. The second one is for moving the tool from the workpiece and unloading it. Due to the definition of residual stress which is the internal equilibrium stress that remains in a component after eliminating the external force or inhomogeneous temperature field, the third step is for the stress relaxation procedure. When the cutting tool is removed, the thermal convection region on the work piece is set. In the last step,

Fig. 2 Thermo-physical and mechanical properties of In718, (**a**) Poisson´s coefficient, (**b**) Young modulus, (**c**) Specific heat, (**d**) Thermal conductivity
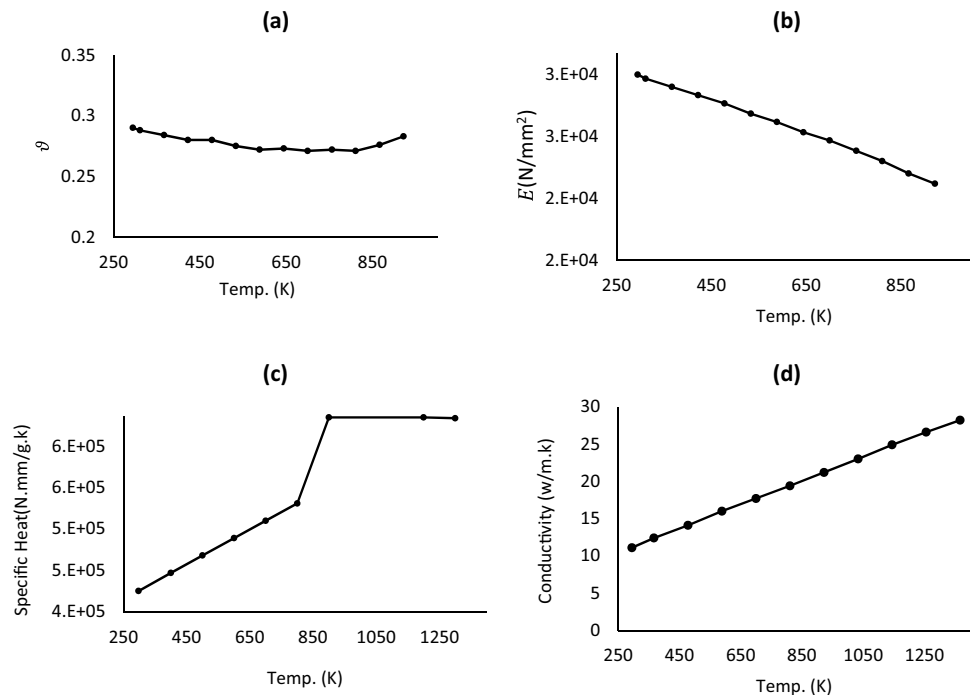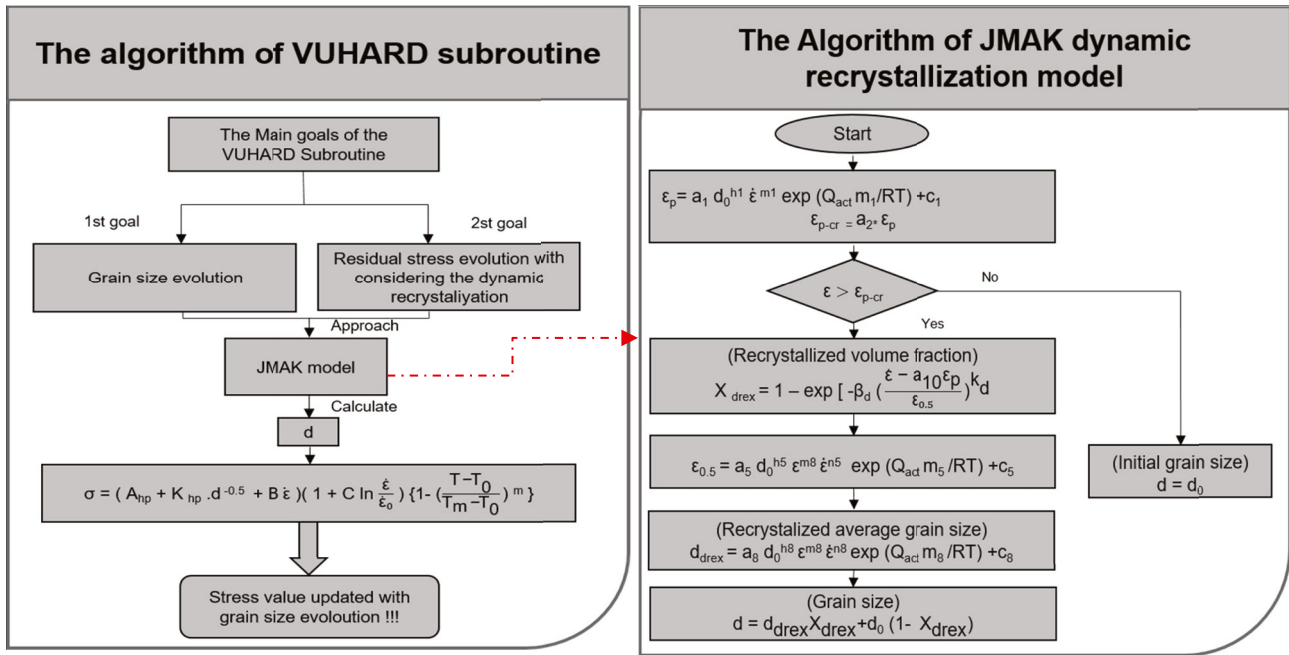
Fig. 3 Algorithm of material modeling and the JMAK DRX model

define a condition that the temperature at which the workpiece is cooled until room temperature. The film coefficient is $10 \frac{W}{m^2} C°$, and the sink temperature is 293K°. The material flow in the Z direction is prohibited while it is allowed in the Y direction. The tool and plate were fixed in terms of velocity and displacement boundary conditions. The degree of freedom for the workpiece is to move with a prescribed cutting velocity against the tool. The material moves from left to right, while the cutting tool does not have any relative movement. Accordingly, boundary conditions (Fig. 1a) for the material are the cutting velocity (V_C) applied on the left side and frictionless support at the bottom. The cutting velocity is assumed constant as an initial condition in the material to be cut. Friction has a profound influence on the simulation results in terms of temperature. In this regard, tangential behavior with penalty friction formulation is
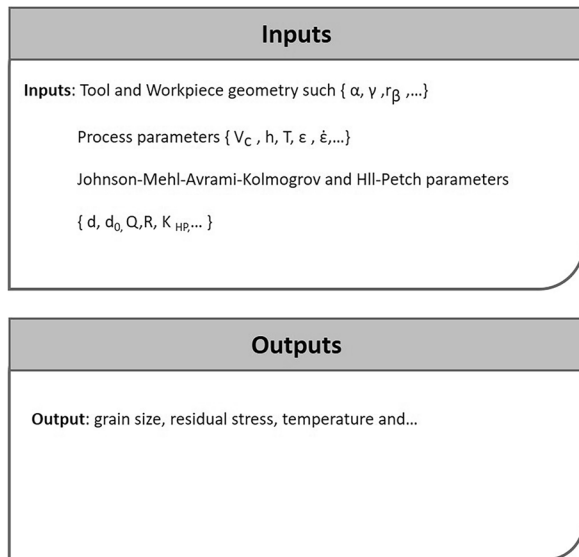
Fig. 4 Implementation of JMAK in the VUHARD subroutine
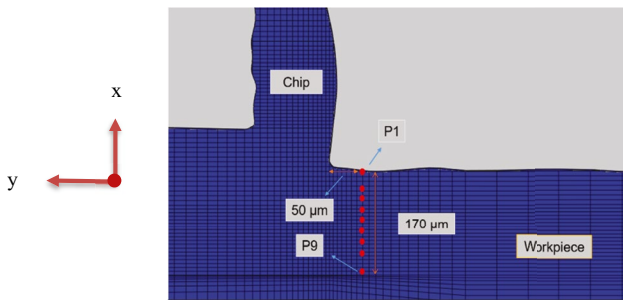
Fig. 5 The position of the points which are measured at the workpiece

defined. For defining friction, temperature-dependent data is implemented. The hard contact pressure overclosure is used to create normal behavior, and pressure-dependency information is used to describe thermal conductance.

4.2 Material module

In this study, Inconel 718 is used for the machining process. Mechanical and physical properties changing by temperature are shown in Table 7 and Fig. 2. Furthermore, the cutting

Fig. 6 Residual stress in feed direction (x-axis) for cutting edge radius with 1μm and cutting velocity $Vc = 150 \text{m/min}$ depth of cut. **a**: $h = 0.06 \text{mm}$, **b** $h = 0.12 \text{mm}$, and **c** $h = 0.2 \text{mm}$
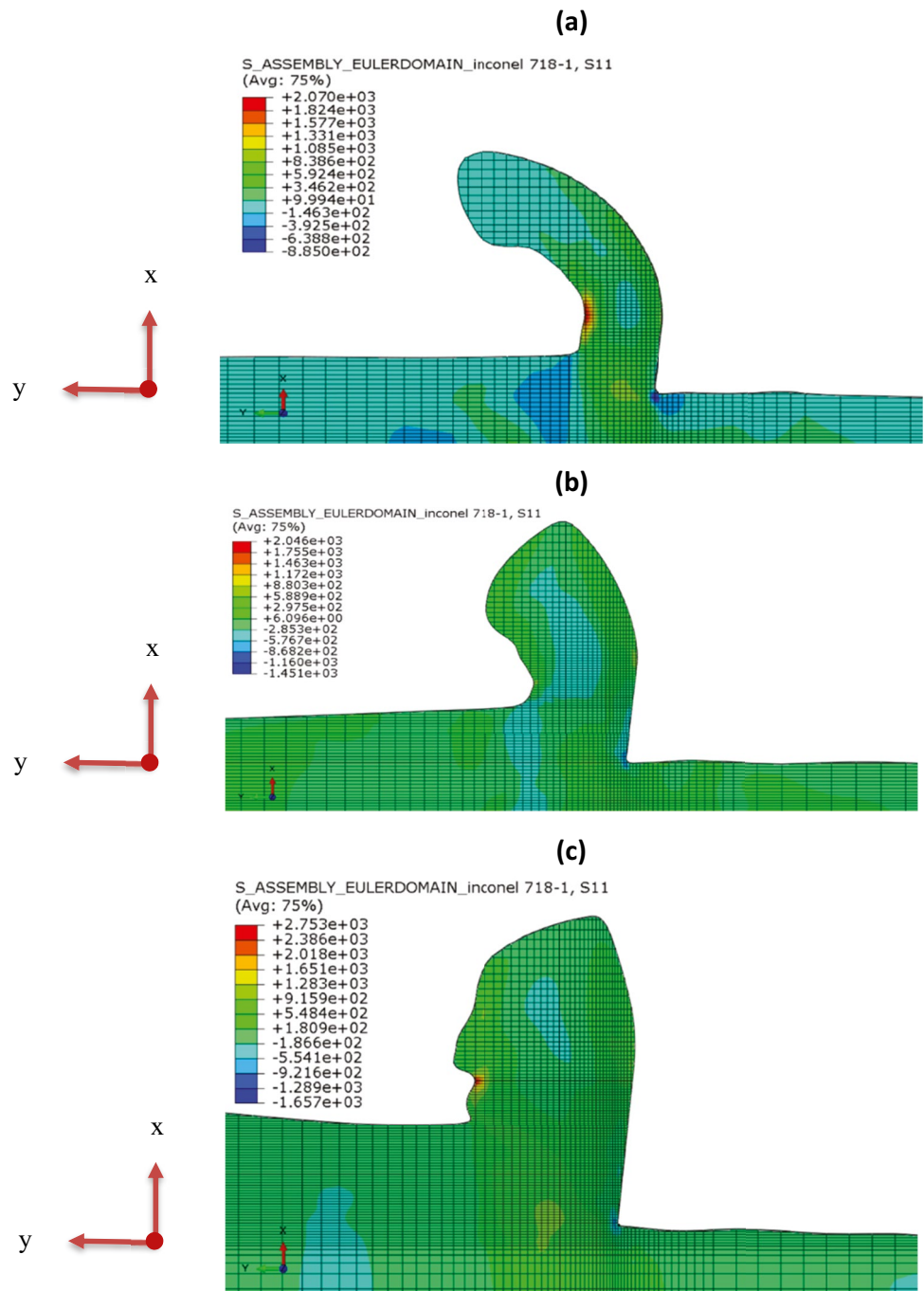
tool is considered Carbide material, and the specification is presented in Table 8 as well.

4.3 FE implementation

The JMAK model is implemented using FORTRAN language in user-defined subroutine VUHARD in ABAQUS-explicit according to the algorithm shown in Fig. 3 to modify the material parameter and call the material parameters in the constitutive model and carry out mechanical calculations. Hereby, the implementation of user codes via the VUHARD subroutine based on the algorithm is shown in Fig. 4. In this spectrum, the peak strain criterion is designed to define the time at which the dynamic recrystallization will happen. When the strain reaches the specified value, the

dynamic recrystallization will start and the size of the grain will be changed. Then taking advantage of other values such as DRX grain size parameters of JMAK, recrystallized volume fraction, and dynamically recrystallized average grain size, the new grain size can be calculated. Resorting to the derived new grain size, embedding in the modified JC flow stress model, the residual stress can be achieved.

5 Results and discussion

In this research, a numerical technique for an orthogonal cutting model with respect to various forces at different cutting conditions is presented using FEM. In the modeling of orthogonal cutting, the VUHARD subroutine runs with 2

Fig. 7 Residual stress in the feed direction (*x*-axis) and cutting velocity 150m/min with cutting-edge radius 1μm at time step 3×10^{-4} in different depths into the work piece for **a** 0.06mm depth of cut, **b** 0.12mm cutting depth, and **c** 0.2mm depth of cut
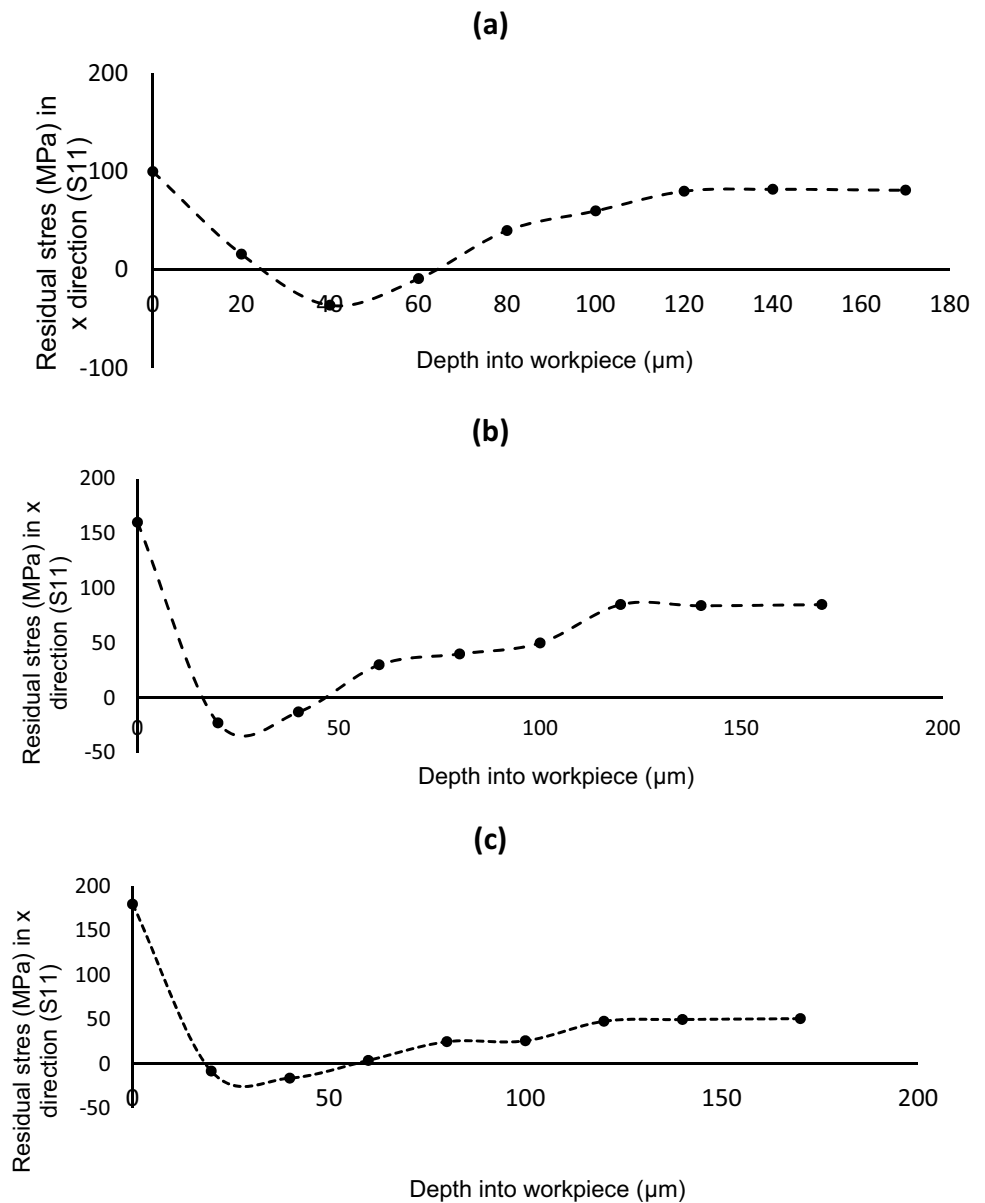
different conditions. In one of them, the cutting edge radius is around 1μm, and in the other one, it is around 70μm. The residual stress evolution in the feed direction (x-axis) and in the cutting velocity direction (y-axis) and Mises residual stress are measured at the points of interest P1 to P9 with the fixed location for each run. In Fig. 5, the position of the group of P points at workpiece is shown. P1 is located at the machined surface, and P1, P2, … and P9 are going into the depth of the workpiece until 170μm. P1 has a 50μm horizontally distance from the cutting edge of the tool.

5.1 Study on the effect of changes in depth of cut on residual stress

Figure 6a–c show the residual stress in the orthogonal cutting process with a cutting edge radius around 1μm for 3 different depth of cut values in the feed direction (x-axis).

The residual stress intensity has a decreasing trend from 2070 to 2046MPa by changing the depth of cut from 0.06 to 0.12mm and then jumping to 2753MPa for 0.2mm.

Fig. 8 Residual stress in the cutting velocity direction (y-axis) for a tool with a 1μm cutting edge radius and cutting velocity $Vc = 150$m/min and depth of cut **a** $h = 0.06$mm, **b** $h = 0.12$mm, and **c** $h = 0.2$mm
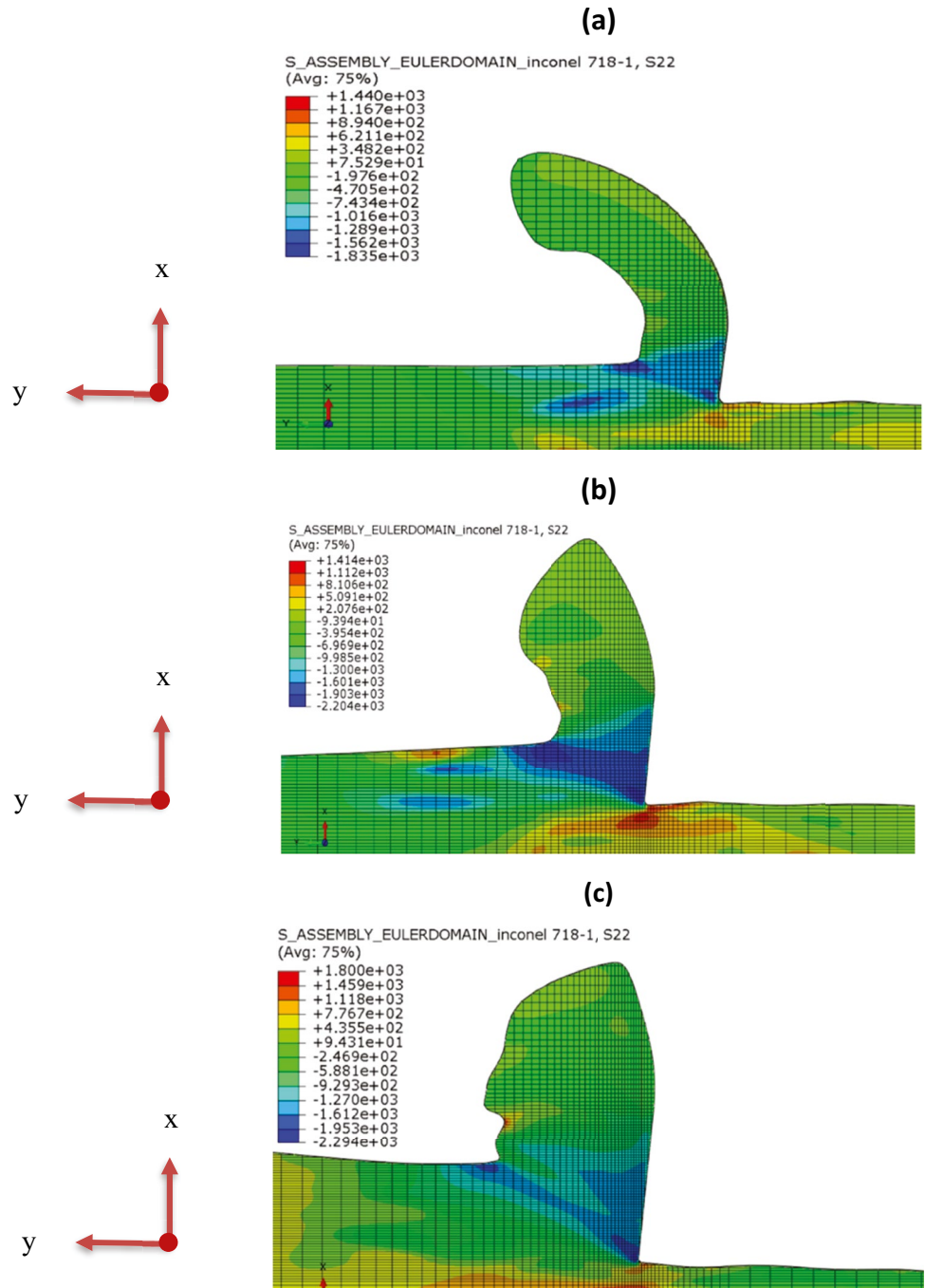
Besides, analysis of the tensile stress at the machined surface of the workpiece specifically in the cutting-edge region shows that there is negative stress in the feed direction (*x* direction) which means that the workpiece is experiencing compressive stress in this aforementioned region.

The residual stress distribution at the machined surface of the workpiece is illustrated in the feed direction (*x* direction) in Fig. 7a–c. The values of tensile stresses decrease as much as the point closer to the cutting edge. Figure 8 presents the residual stress in the cutting velocity direction (*y* direction) for the tool with 1 µm cutting edge radius and various depth of cut values including *h* = 0.06mm, 0.12mm, and 0.2mm with cutting velocity *Vc* = 150m/min. Besides, the stress condition on the velocity direction also has both positive (tensile) and negative (compression) values based on Fig. 9. As the point closes to the cutting edge, the compressive stress is increased.

Fig. 9 Residual stress in cutting velocity direction (*y*-axis) and cutting velocity 150m/min with cutting edge radius 1µm at time step 3×10^{-4}s in different depths into the workpiece for **a** 0.06mm depth of cut, **b** 0.12mm cutting depth, **c** 0.2mm depth of cut
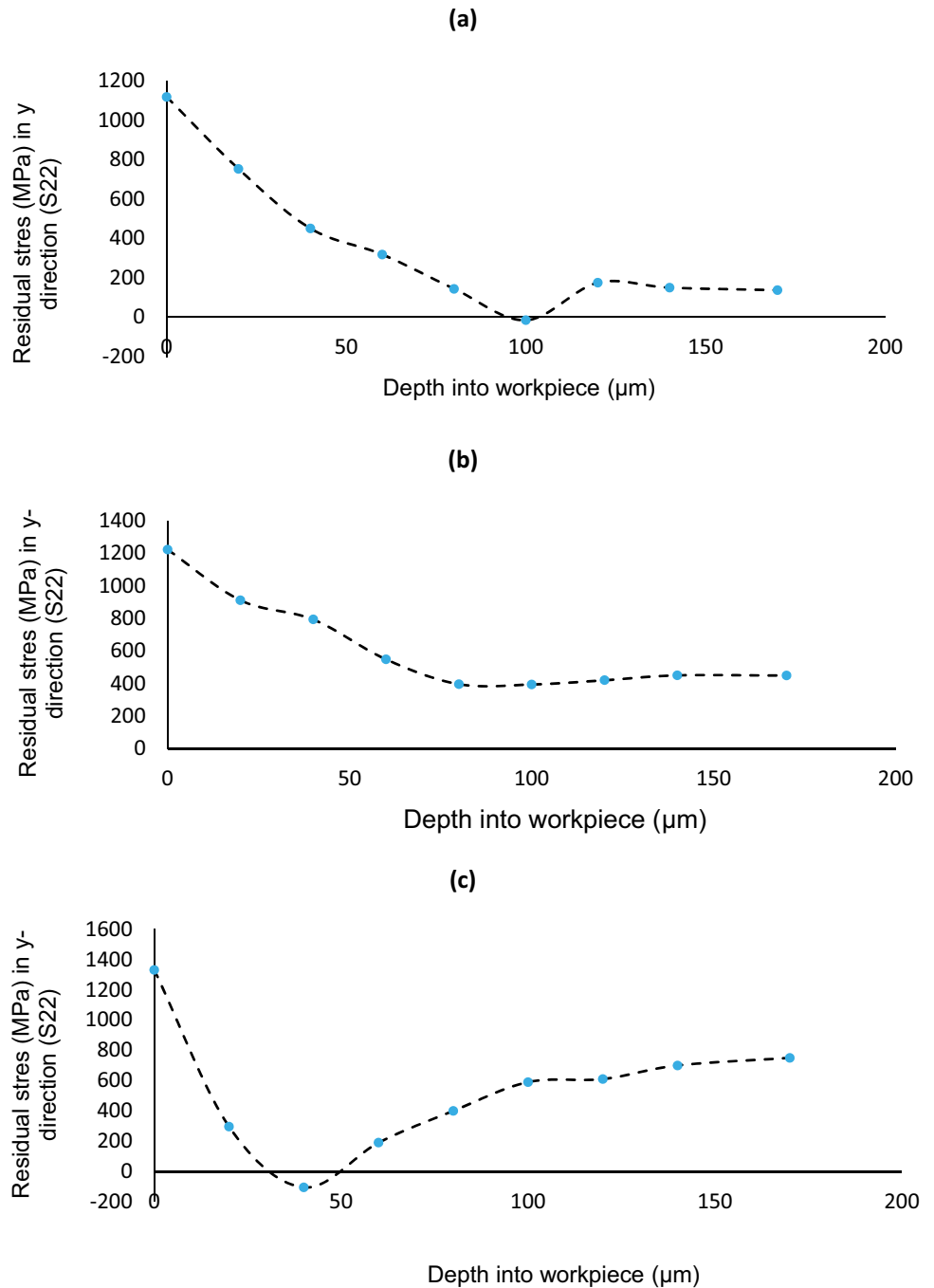
Fig. 10 Mises residual stress for tool with 1 μm cutting edge radius and cutting velocity $Vc = 150 \text{m/min}$ and depth of cut **a** $h = 0.06 \text{mm}$, **b** $h = 0.12 \text{mm}$, and **c** $h = 0.2 \text{mm}$
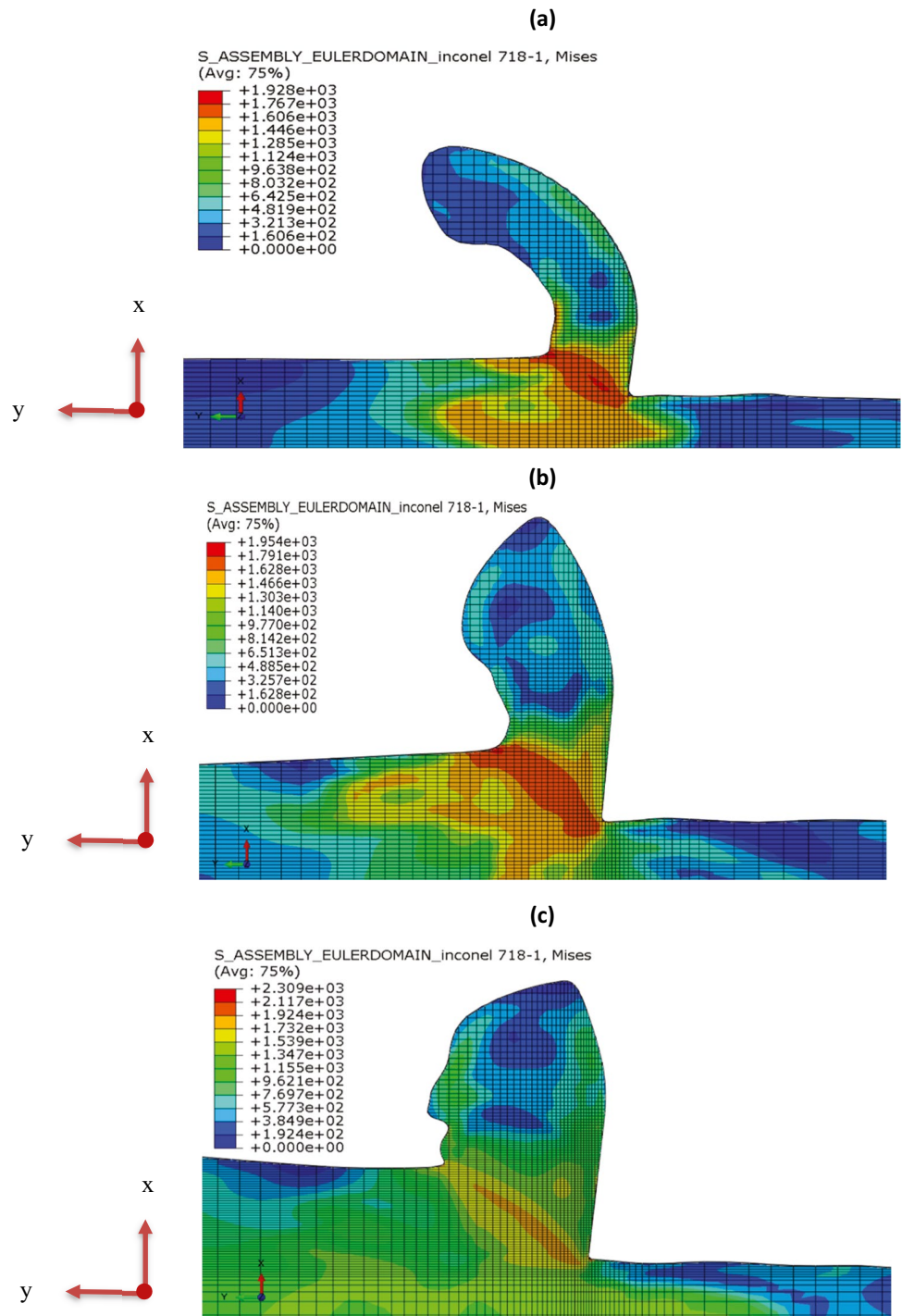
In Fig. 10a–c, the Von-Mises stress values are presented for three different depths of cut values including $h = 0.06 \text{mm}, 0.12 \text{mm}$, and 0.2mm. It can be seen that all values in this picture are positive and as much as the point is closer to the cutting edge, the value of stress has an increasing trend. The results reveal that the maximum value of the stress happens at the primary shear zone where the stress value is maximum. Furthermore, the Von-Mises stress increases as the depth of cut increases.
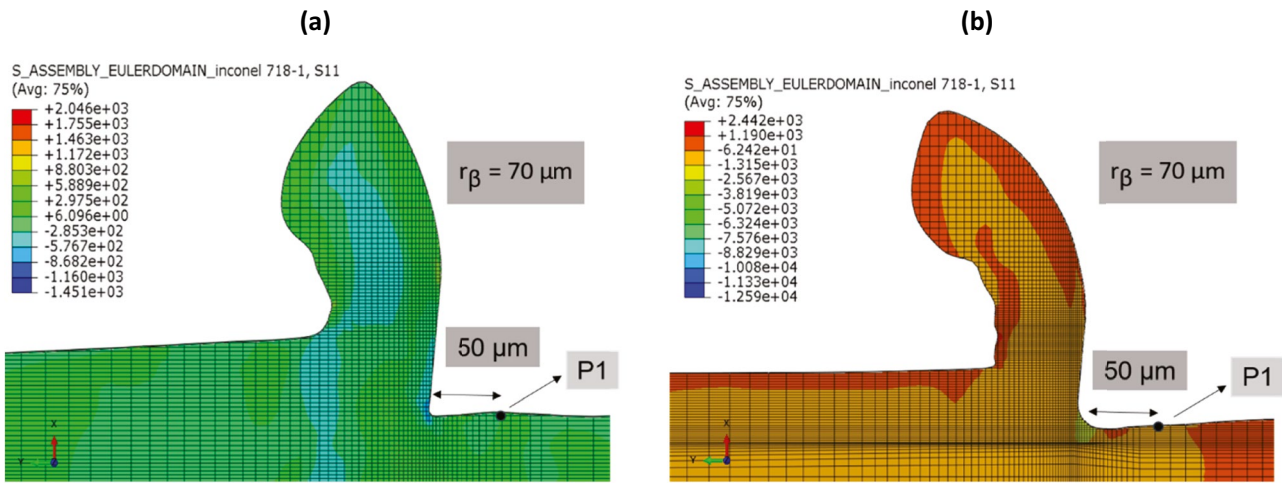
Fig. 11 Residual stress in the feed direction (*x*-axis) with depth of cut 0.06mm and cutting velocity 150m/min for cutting edge radius **a** 1μm and **b** 70μm at time step 3×10^{-4}s

5.2 Study the effect of changing in cutting edge radius on residual stress

To reveal the effect of the cutting edge radius in the orthogonal cutting process, this sort of simulation runs with a cutting edge radius of 70μm. Figure 11a and b show the effect of changing the cutting edge radius on the residual stress in the feed direction (*x*-axis) with a cutting speed of 150m/min. The comparison between Fig. 11a and b shows that there is much more compression in the workpiece which is produced with a cutting edge radius of 1μm. The same comparative study was done in the direction of cutting velocity in Fig. 12a, b to shed some light on the effect of changing the

cutting edge radius on the residual stress in the cutting velocity direction when it has 50m/min cutting velocity. Having the same cutting edge radius and increasing the cutting velocity leads to an increase in the residual stress.

5.3 Study on the grain size evolution

Regarding the key role function of the cutting parameters like cutting edge radius and cutting velocity on the final grain size of machined workpieces, this section of the study focuses on figuring out their functions. Figure 13a and b show the derived grain evolution size variation by a
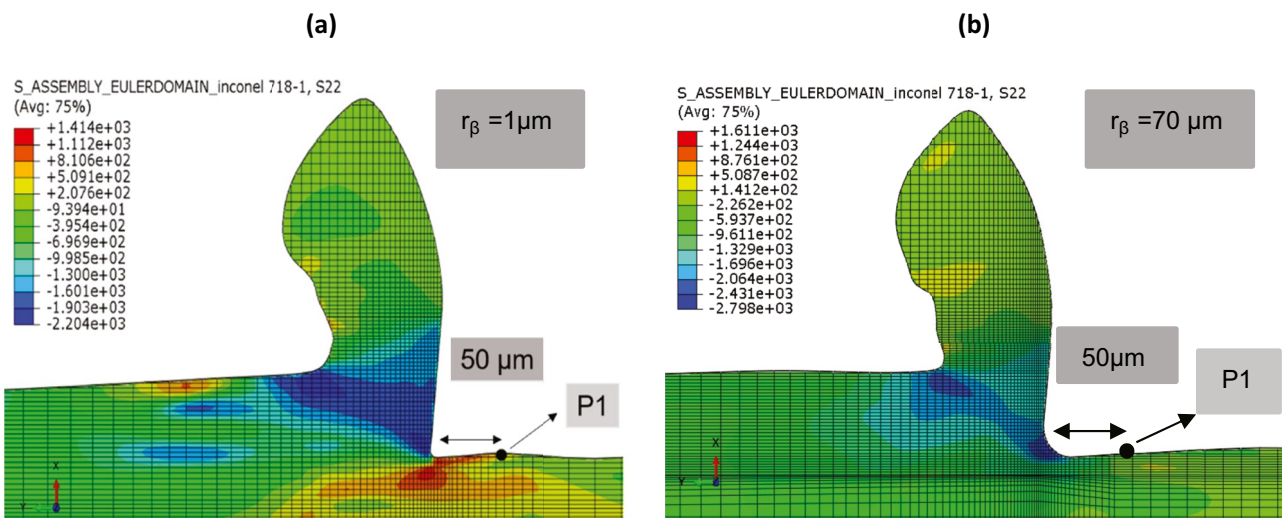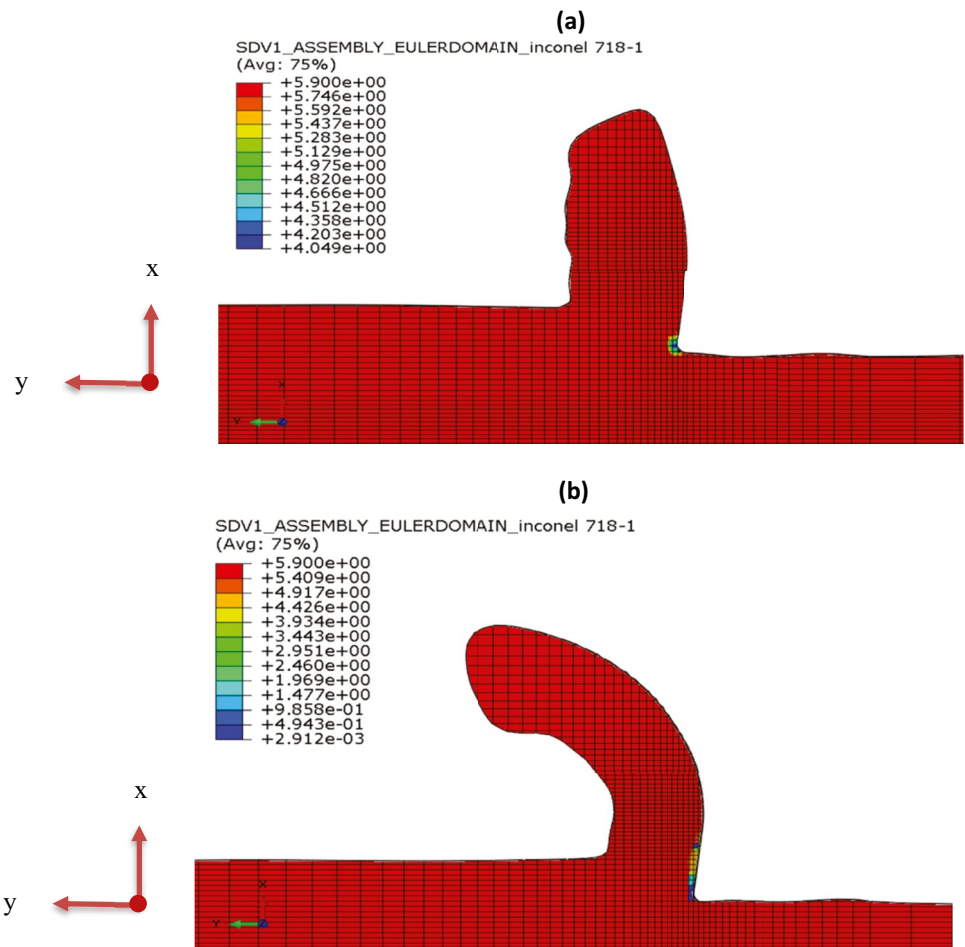

Fig. 12 Residual stress in cutting velocity direction (*y*-axis) with depth of cut 0.06mm and cutting velocity 50m/min for cutting edge radius **a** 1μm and **b** 70μm at time step 3×10^{-4}s

Fig. 13 Grain size evolution for depth of cut $h = 0.06$mm and for a tool with 1μm radius, **a** cutting velocity $Vc = 50$m/min, **b** cutting velocity $Vc = 150$m/min

(a)

(b)

constant value of cutting edge radius 1μm and changing the cutting velocity from $Vc = 50$m/min to $Vc = 150$m/min. The results show that the grain size change region is limited to the area around the cutting edge of the tool, especially on the side of the chip. Accompanied by increasing cutting velocity, it is expected to get a larger grain size change domain.

The effect of the cutting speed on the evolution of grain size is shown in Fig. 14 for different depths of cut for cutting edge radius 1μm. By increasing the cutting velocity, the area of grain size evolution is increased. Nevertheless, the region of the grain size change is limited to the chip region, and the region with grain size change at the machined surface of the workpiece is very small.

By changing the cutting edge radius, Fig. 15a and b present the effect of this parameter on the grain size evolution. Moreover, it can be seen by increasing the cutting velocity that the affected area by recrystallized grain has an increasing trend.

The grain size distribution is shown in Fig. 16 to investigate the effect of the cutting velocity on the grain size domain briefly with a constant cutting edge radius.

To evaluate the spatial effect on the grain size distribution, the mesh size changed to 4μm. It must be mentioned here that, to keep track of this parameter, the mesh size must be smaller than the initial grain size. For this purpose, a mesh size of 4μm is used. It can be seen obviously that the results are much more visible with a smaller mesh size as shown in Fig. 17.

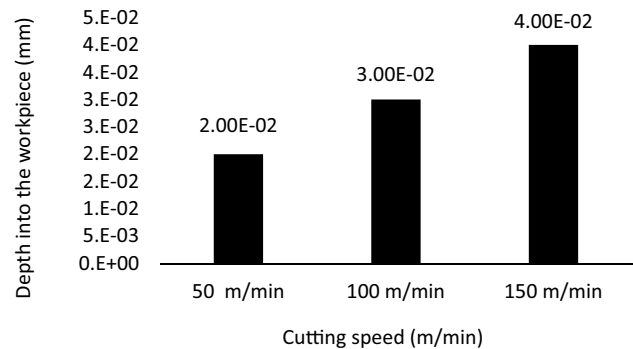**Fig. 14** Grain size change depth into the workpiece for $h = 0.06$mm depth of cut for cutting edge radius 1μm

Fig. 15 Grain size evolution for depth of cut $h = 0.06$mm and for a tool with 70μm radius, **a** cutting velocity $Vc = 50$m/min, **b** cutting velocity $Vc = 150$m/min

(a)

(b)
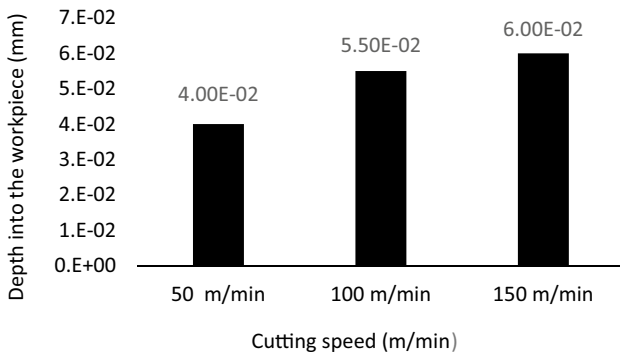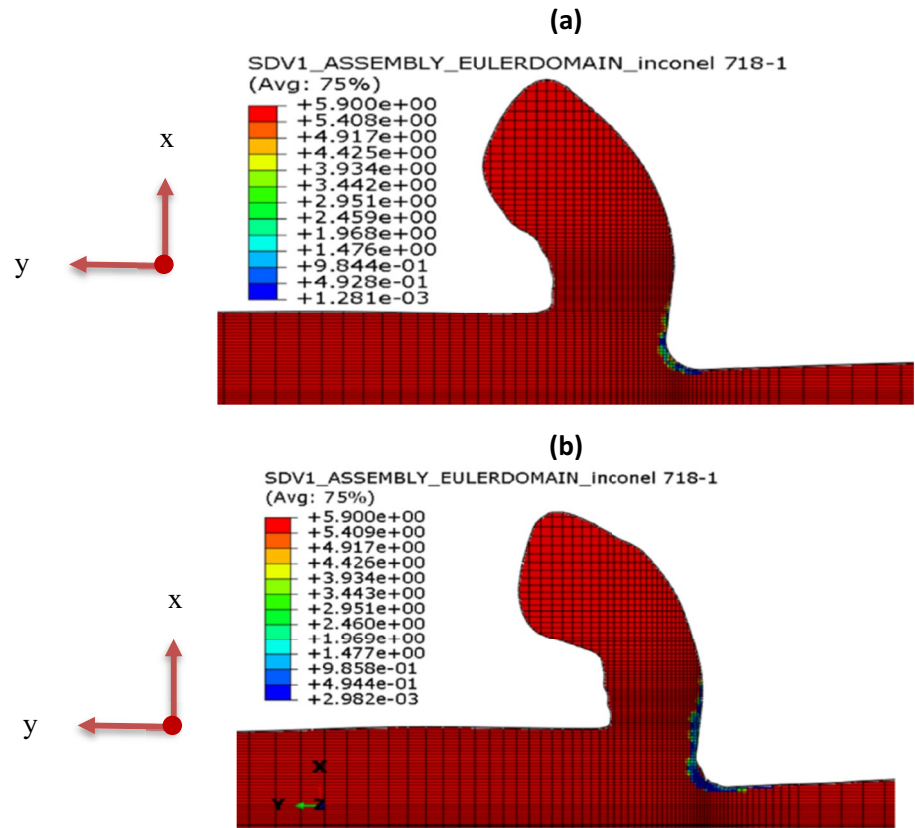
Fig. 16 Grain size change depth into the workpiece for $h = 0.06$mm cutting depth for cutting edge radius 70μm

5.4 Study on the temperature evolution

Because induced defects are most likely created by a combination of factors such as cutting conditions, tool shape, and machining temperatures, all of which contribute to residual stress, investigating the effect of temperature evolution is crucial. Figure 18a and b illustrate the temperature distribution in various conditions. The results show that the temperature increases with the augmentation of velocity at the constant depth of cut.

The interaction between key parameters like cutting velocity and depth of cut and their effect on the temperature evolution is shown in Fig. 19.

Fig. 17 Grain size evolution for a tool with 70μm cutting edge radius with depth of cut $h = 0.06$mm and cutting velocity $Vc = 50$m/min with finer mesh 4μm

Fig. 18 Temperature evolution (K) for tool with 1μm cutting edge radius for depth of cut $h = 0.06$mm with **a** cutting velocity $Vc = 50$m/min, **b** cutting velocity $Vc = 150$m/min

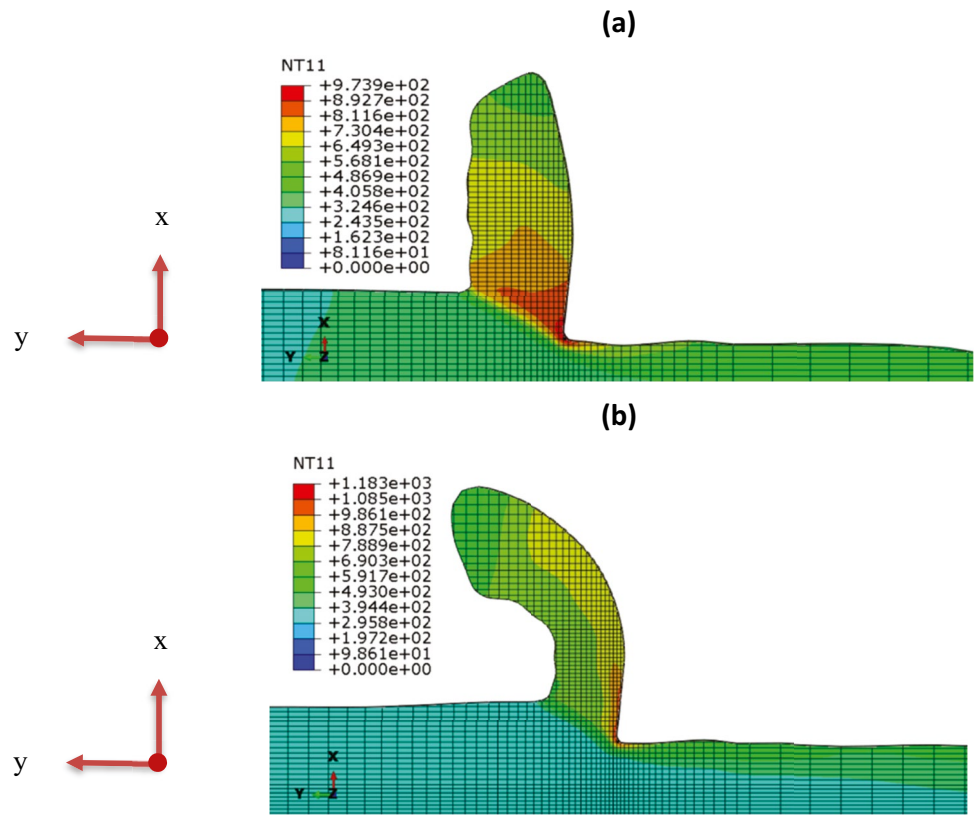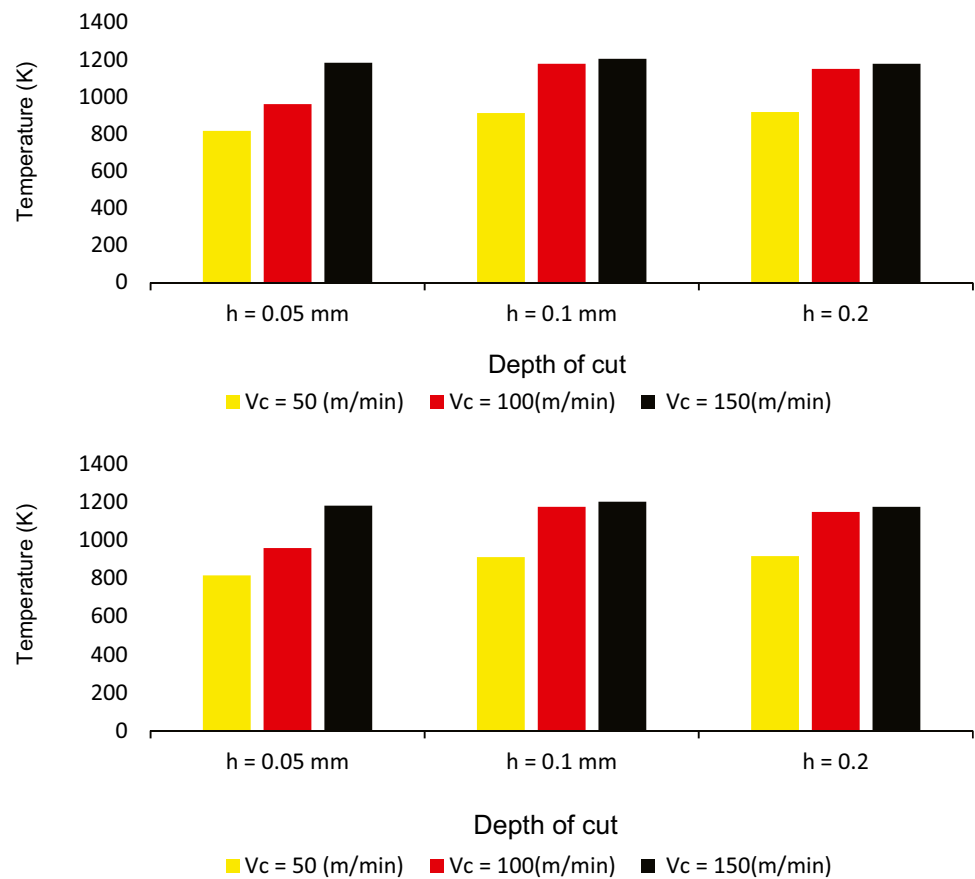**Fig. 19** Temperature evolution based on depth of cut and cutting velocity for cutting-edge radius 1μm

6 Conclusion

This paper is concerned with the challenge of developing a proper material law, which is capable to consider the DRX effect that happens in a high-temperature process. Due to the specific range of temperature in the cutting process, a recrystallization effect may occur. To predict the induced residual stress and DRX, the FE commercial software ABAQUS-explicit is utilized and the VUHARD user sub-routine is developed to illustrate the material model in the plastic zone of Inconel 718. To demonstrate the workpiece rim zone modifications, the CEL approach is implemented. Monitoring the residual stress as the main factor influencing fatigue life of machined components and grain size as a crucial parameter in the mechanics of material, it is possible to define a more realistic safety criterion. The grain size effect on the material flow stress behavior is included by adding the grain size–dependent term into the traditional JC model. The JMAK model calculates the recrystallized volume fraction and grain size as a function of strain, strain rate, and temperature. The average grain size is calculated with a rule of the mixture by volume. The proposed model is employed to investigate the effect of the key features of the orthogonal cutting process including cutting velocity, depth of cut, and cutting edge radius on the residual stress and grain evolution, as well as the affected domain. With cutting edge radius 1μm and cutting velocity 150m/min, by changing the chip thicknes values from 0.06 to 0.12 mm, the stress intensity firstly decreases, and then by increasing from 0.12 to 0.2mm, there is an increasing trend in stress intensity. The closer points to the cutting edge lead to an increase in the compressive stress, and the maximum value belongs to the primary shear zone where the stress value is maximum. On the other hand, the effect of changing the cutting edge radius on the residual stress in the feed direction is studied. The results illustrate that for the constant cutting velocity and depth of cut, increasing the cutting edge radius leads to an increase in the residual stress. The grain size varies by changing the cutting speed, so that increasing the cutting velocity induces more temperature evolution, consequently increasing residual stress.

The model provides significant improvement in the calculation of residual stress in machined surfaces to achieve the desired fatigue life and optimize the machining process parameters. Future directions in the scope of the present research can be outlined with a comparative study with JC material modeling to shed the light on the effect of the proposed execution efficiency of the results with the experiment-driven data.

Availability of data and materials It has been confirmed that data is open and transparent.

Code availability Not applicable.

Declarations

Ethics approval Not applicable.

Consent to participate Not applicable.

Consent for publication Not applicable.

Conflict of interest The authors declare no competing interests.

References

1. Kirka MM, Plotkowski A, Nandwana P, Chaudhary A, Babu SS, Dehoff RR (2018) Progress in the processing and understanding of alloy 718 fabricated through powder bed additive manufacturing processes. ISBN:9783319894799

2. Aydogan B, O'Neil A, Sahasrabudhe H (2021) Microstructural and mechanical characterization of stainless steel 420 and Inconel 718 multi-material structures fabricated using laser directed energy deposition. J Manuf Process 68:1224–1235. https://doi.org/10.1016/j.jmapro.2021.06.031

3. Blakey-Milner B, Gradl P, Snedden G, Brooks M, Pitot J, Lopez E, Leary M, Berto F, du Plessis A (2021) Metal additive manufacturing in aerospace: A review. Mater Des 209:110008. https://doi.org/10.1016/j.matdes.2021.110008

4. Thellaputta GR, Chandra PS, Rao CSP (2017) Machinability of nickel based superalloys: a review. Mater Today Proc 4:3712–3721. https://doi.org/10.1016/j.matpr.2017.02.266

5. Bartarya G, Choudhury SK (2012) State of the art in hard turning. Int J Mach Tools Manuf 53:1–14. https://doi.org/10.1016/j.ijmachtools.2011.08.019

6. Rahimi S, Violatos I (2021) Comparison between surface and near-surface residual stress measurement techniques using a standard four-point-bend specimen. Exp Mech. https://doi.org/10.1007/s11340-021-00779-6

7. Sarıkaya M, Gupta MK, Tomaz I, Pimenov DY, Kuntoğlu M, Khanna N, Yıldırım ÇV, Krolczyk GM (2021) A state-of-the-art review on tool wear and surface integrity characteristics in machining of superalloys. CIRP J Manuf Sci Technol 35:624–658. https://doi.org/10.1016/j.cirpj.2021.08.005

8. Ye C, Zhang C, Zhao J, Dong Y (2021) Effects of post-processing on the surface finish, porosity, residual stresses, and fatigue performance of additive manufactured metals: a review. J Mater Eng Perform 30:6407–6425. https://doi.org/10.1007/s11665-021-06021-7

9. Jiang H, Ren Z, Yi Y, He L, Yuan S (2021) Effect of machining on performance enhancement of superficial layer of high-strength alloy steel. J Mater Res Technol 14:1065–1079. https://doi.org/10.1016/j.jmrt.2021.07.028

10. Liu Y, Xu D, Agmell M, Saoubi RM, Ahadi A, Stahl JE, Zhou J (2021) Numerical and experimental investigation of tool geometry effect on residual stresses in orthogonal machining of Inconel 718. Simul Model Pract Theory 106:102187. https://doi.org/10.1016/j.simpat.2020.102187

11. Curtis D, Krain H, Winder A, Novovic D (2021) Impact of grinding wheel specification on surface integrity and residual stress when grinding Inconel 718. Proc Inst Mech Eng Part B J Eng Manuf 235:1668–1681. https://doi.org/10.1177/0954405420961209

12. Assessment EA, Hauk V, Behnken H, Genzel C, Pfeiffer W, Pintschovius L, Reimers W, Schneider E, Schottes B, Theiner WA (1997) Structural and residual stress analysis by nondestructive methods. Struct Residual Stress Anal Nondestruct Methods

13. Hashmi S (2014) Comprehensive Materials Processing 1. ISBN: 9780080965338

14. Elsheikh AH, Shanmugan S, Muthuramalingam T, Thakur AK, Essa FA, Ibrahim AMM, Mosleh AO (2021) A comprehensive review on residual stresses in turning. Adv Manuf. https://doi.org/10.1007/s40436-021-00371-0

15. Thakur DG, Ramamoorthy B, Vijayaraghavan L (2012) Effect of cutting parameters on the degree of work hardening and tool life during high-speed machining of Inconel 718. Int J Adv Manuf Technol 59:483–489. https://doi.org/10.1007/s00170-011-3529-6

16. Madyira DM, Laubscher RF, Janse Van Rensburg N, Henning PFJ (2013) High speed machining induced residual stresses in Grade 5 titanium alloy. Proc Inst Mech Eng Part L J Mater Des Appl 227:208–215. https://doi.org/10.1177/1464420712462319

17. M'Saoubi R, Outeiro JC, Changeux B, Lebrun JL, Morão Dias A (1999) Residual stress analysis in orthogonal machining of standard and resulfurized AISI 316L steels. J Mater Process Technol 96:225–233. https://doi.org/10.1016/S0924-0136(99)00359-3

18. Hua Y, Liu Z (2018) Effects of cutting parameters and tool nose radius on surface roughness and work hardening during dry turning Inconel 718. Int J Adv Manuf Technol 96:2421–2430. https://doi.org/10.1007/s00170-018-1721-7

19. Sasahara H (2005) The effect on fatigue life of residual stress and surface hardness resulting from different cutting conditions of 0.45%C steel. Int J Mach Tools Manuf 45:131–136. https://doi.org/10.1016/j.ijmachtools.2004.08.002

20. Jaap S (2001) Fatigue of Structures and Materials, 2nd ed, vol 21. Springer, Dordrecht. ISBN: 978-1-4020-6808-9

21. Rule WK, Jones SE (1998) A revised form for the Johnson-Cook strength model. Int J Impact Eng 21:609–624. https://doi.org/10.1016/S0734-743X(97)00081-X

22. Johnson GR, Cook WH (1983) A Computational constitutive model and data for metals subjected to large strain, high strain rates and high pressures. Seventh Int Symp Ballist 541–547

23. Huang D, Wu WT, Lambert D, Semiatin SL (2001) Computer simulation of microstructure evolution during hot forging of waspaloy and nickel alloy 718. Microstructure Modeling and Prediction During Thermomechanical Processing 137–146

24. Johansson J, Persson C, Lai H, Hörnqvist Colliander M (2016) Microstructural examination of shear localisation during high strain rate deformation of Alloy 718. Mater Sci Eng A 662:363–372. https://doi.org/10.1016/j.msea.2016.03.080

25. Pan Z, Feng Y, Lu YT, Lin YF, Hung TP, Hsu FC, Liang SY (2017) Force modeling of Inconel 718 laser-assisted end milling under recrystallization effects. Int J Adv Manuf Technol 92:2965–2974. https://doi.org/10.1007/s00170-017-0379-x

26. Pan Z, Liang SY, Garmestani H, Shih DS (2016) Prediction of machining-induced phase transformation and grain growth of Ti-6Al-4 V alloy. Int J Adv Manuf Technol 87:859–866. https://doi.org/10.1007/s00170-016-8497-4

27. Jafarian F, Imaz Ciaran M, Umbrello D, Arrazola PJ, Filice L, Amirabadi H (2014) Finite element simulation of machining Inconel 718 alloy including microstructure changes. Int J Mech Sci 88:110–121. https://doi.org/10.1016/j.ijmecsci.2014.08.007

28. Reyes LA, Páramo P, Salas Zamarripa A, de la Garza M, Guerrero-Mata MP (2016) Influence of Processing Parameters on Grain Size Evolution of a Forged Superalloy. J Mater Eng Perform 25:179–187

29. Loyda A, Hernández-Muñoz GM, Reyes LA, Pb Zambrano-Robledo (2016) Microstructure modeling of a Ni-Fe-based superalloy during the rotary forging process. J Mater Eng Perform 25:2128–2137

30. Tekkaya B, Meurer M, Münstermann S (2020) Modelling of grain size evolution with different approaches via FEM when hard machining of AISI 4140. Metals 10:1–20